Journal of the Taiwan Institute of Chemical Engineers 188 (2026) 106890

Contents lists available at ScienceDirect

Journal of the Taiwan Institute of Chemical Engineers

journal homepage: www.journals.elsevier.com/journal-of-the-taiwan-institute-of-chemical-engineers

Synergistic Pr-Mo-O@f-MWCNT heterointerfaces for ultrasensitive electrochemical detection of fenitrothion in complex environmental and food samples

Sri Balaji Natarajan [b,1], Kumar Gokulkumar [a,1], Shen-Ming Chen [b,*], Shih-Hsuan Chen [a], Kun-Mu Lee [a,c,d,e,*]

[a] Center for Sustainability and Energy Technologies, Chang Gung University, Taoyuan, 33302, Taiwan
[b] Department of Chemical Engineering and Biotechnology, National Taipei University of Technology, Taipei, Taiwan
[c] Department of Chemical and Materials Engineering, Chang Gung University, Taoyuan, 33302, Taiwan
[d] Division of Neonatology, Department of Pediatrics, Chang Gung Memorial Hospital, Linkou, Taoyuan, 33305, Taiwan
[e] College of Environment and Resources, Ming Chi University of Technology, New Taipei 24301, Taiwan

ARTICLE INFO

Keywords:
Praseodymium–molybdate oxide
Fenitrothion detection
Electrochemical sensing
Food and environmental monitoring

ABSTRACT

Background: Fenitrothion (FT) is a widely used organophosphorus pesticide whose persistent residues in environmental waters and food systems pose significant risks due to their neurotoxic effects. Therefore, the development of sensitive and reliable analytical platforms for fenitrothion monitoring is essential for environmental surveillance and food safety applications.

Methods: In this study, a praseodymium–molybdate oxide/functionalized multi-walled carbon nanotube (PrMo–O@f-MWCNT) hybrid composite was developed as an electrocatalytic sensing platform for fenitrothion (FT) detection. The Pr–Mo–O component provides abundant redox-active sites and defect-rich oxygen environments, while the conductive f-MWCNT network enhances electron transport and accelerates interfacial charge transfer. The composite was characterized by XRD, FESEM, TEM, EDS mapping, and XPS analyses. Electrochemical performance of the modified electrode was investigated using cyclic voltammetry (CV), electrochemical impedance spectroscopy (EIS), and differential pulse voltammetry (DPV).

Main findings: The proposed sensor exhibited a wide linear detection range of to 1 μM and to 1845 μM, with a low detection limit of 0.047 μM. The Pr-Mo-O@f-MWCNT-modified electrode also demonstrated excellent selectivity, stability, and reproducibility toward fenitrothion detection. Practical applicability was successfully validated in river water, soil, tomato, and cabbage samples, achieving satisfactory recoveries in the range of 98.2–101.4% with low RSD values. The simple fabrication strategy and strong analytical performance highlight the potential of this platform for integrated environmental surveillance and advanced food safety monitoring of pesticide residues.

1. Introduction

The extensive use of synthetic insecticides has played a key role in protecting crops and supporting agricultural productivity; however, their widespread application has also introduced serious environmental and food safety challenges [1–3]. Among these chemicals, organophosphorus compounds are of particular concern due to their high biological activity and potential toxicity [4,5]. Within this class, Fenitrothion (FT) has been applied for several decades in agriculture, forestry, and public health programs because of its strong insecticidal efficiency and cost-effectiveness [6]. Structurally, FT contains a phosphorothioate group linked to a nitrophenyl moiety, a configuration that enables effective pest control but also contributes to its chemical instability and formation of toxic transformation products [7–9]. After application, FT residues can persist in agricultural soils, adsorb onto plant surfaces, and migrate through runoff and leaching into surface and groundwater systems [10,11]. These residues may accumulate in edible crops and aquatic organisms, increasing the risk of bioaccumulation and

* Corresponding authors.
E-mail addresses: smchen1957@gmail.com (S.-M. Chen), kmlee@mail.cgu.edu.tw (K.-M. Lee).
[1] These authors contributed equally to this work.

https://doi.org/10.1016/j.jtice.2026.106890
Received 16 March 2026; Received in revised form 27 May 2026; Accepted 22 June 2026
Available online 10 July 2026

trophic transfer [12]. Moreover, FT is known to interfere with enzymatic systems in non-target organisms, disrupt aquatic ecosystems, and generate degradation byproducts that exhibit equal or greater toxicity than the parent compound [13]. Continuous exposure to FT residues through contaminated food and water has been associated with adverse health effects, raising serious concerns over long-term dietary intake [14]. Taken together, the persistence, toxicity, environmental mobility, and food chain transfer of FT highlight its significant disadvantages and underscore the urgent need for continuous and reliable monitoring to ensure food safety, environmental protection, and public health preservation.

Conventional analytical techniques such as gas chromatography–mass spectrometry (GC–MS), liquid chromatography mass spectrometry (LC–MS) [15], and surface-enhanced Raman scattering (SERS) [16] are widely used for pesticide residue analysis because of their high sensitivity and accuracy. However, these approaches typically require costly instrumentation, complex sample preparation, and extended analysis times, limiting their suitability for rapid or on-site food safety assessment [17,18]. In response to these limitations, electrochemical sensing strategies have gained increasing interest due to their simplicity, fast response, low operational cost, and compatibility with portable systems [19,20]. The performance of electrochemical sensors is strongly influenced by the properties of the working electrode surface, which governs electron transfer and analyte interaction. Electrochemical techniques such as cyclic voltammetry and differential pulse voltammetry are commonly employed to probe redox behavior and achieve sensitive quantification, making them attractive for trace-level monitoring of hazardous residues [21–26].

In recent years, Rare-earth-based metal oxides have attracted considerable interest in electrochemical applications owing to their unique electronic configurations, variable oxidation states, and strong chemical stability [27,28]. In parallel, molybdate oxides are recognized for their favourable redox activity and efficient electron transport properties arising from the Mo–O framework [29]. The integration of rare-earth elements with molybdate units offers a rational strategy to construct functional oxides with enhanced electrochemical characteristics [30]. In this context, Praseodymium–molybdate oxide (Pr–Mo–O) represents a distinctive rare-earth molybdate oxide, in which the redox-active molybdenum centers are coupled with the reversible valence states of praseodymium, generating multiple electrochemically active sites [31]. The Mo–O subunits facilitate rapid electron transfer during redox processes, while the Pr^{3+}/Pr^{4+} couple provides additional charge compensation pathways that improve catalytic efficiency [32]. Furthermore, the robust oxide lattice of (Pr–Mo–O) ensures high structural stability and resistance to chemical degradation, while oxygen vacancies and lattice defects promote strong interactions with electroactive species, leading to enhanced adsorption and efficient signal transduction [33].

Carbon-based nanomaterials, particularly multi-walled carbon nanotubes (MWCNTs), are extensively employed in electrochemical applications owing to their outstanding electrical conductivity, large specific surface area, and efficient charge transport characteristics [34–36]. The one-dimensional tubular structure of MWCNTs provides continuous electron pathways that facilitate rapid signal propagation at the electrode interface. However, pristine MWCNTs often suffer from strong agglomeration and limited surface functionality, which reduce their dispersibility and interfacial interaction with other active materials. Chemical functionalization introduces oxygen-containing groups such as carboxyl (–COOH) and hydroxyl (–OH) moieties onto the MWCNT surface, significantly enhancing hydrophilicity, dispersion stability, and surface reactivity [37,38]. These functional groups promote stronger interfacial bonding, improve electron mobility across heterogeneous interfaces, and create additional adsorption sites for electroactive species. Consequently, functionalized MWCNTs enable improved charge transfer efficiency, enhanced electrode stability, and more reliable electrochemical performance [39]. Rare-earth molybdate oxides and carbon nanotube-based materials have individually been explored in electrochemical systems, their interfacial coupling for fenitrothion sensing remains largely unexplored. In particular, the integration of defect-rich Pr–Mo-O with a functionalized MWCNT network can create a synergistic oxide carbon heterointerface that simultaneously enhances catalytic activity, analyte adsorption, and long-range electron transport.

In this work, praseodymium molybdate (Pr–Mo–O) was directly combined with functionalized multi-walled carbon nanotubes (f-MWCNTs) to construct a synergistic hybrid interface for the electrochemical detection of the hazardous pesticide fenitrothion. The intimate integration of Pr–Mo–O with the conductive f-MWCNT network creates a continuous electron-transfer framework and a high-density electroactive surface, enabling efficient analyte adsorption and signal amplification. To the best of our knowledge, this represents the first application of a Pr–Mo–O@f-MWCNT composite for fenitrothion sensing. The Pr–Mo–O@f-MWCNT-modified glassy carbon electrode exhibited wide linear response ranges 1 μM and to 1845 μM, with a low detection limit of 0.047 μM. These enhanced analytical performances originate from the synergistic integration of Pr–Mo–O with the f-MWCNT network, which accelerates interfacial electron transport and reinforces analyte electrode interactions. Importantly, the sensor exhibited reliable and consistent performance in environmental water, soil, and food-derived samples, demonstrating its robustness and practical suitability for pesticide residue determination. This study highlights the promise of advanced hybrid nanomaterials as effective electrochemical platforms for integrated environmental surveillance, food quality control, safety assessment, and on-site monitoring of agricultural contaminants.

2. Chemicals and methods

All reagents employed in this work were of analytical grade and procured from commercial suppliers (Sigma-Aldrich). The chemicals were used as received without any additional purification. Comprehensive details regarding the list of chemicals, preparation of buffer solutions, and the instrumentation utilized in this study are provided in the Supporting Information Sections S1 and S2.

2.1. Synthesis of Pr–Mo–O

In a typical synthesis, an aqueous solution of praseodymium (III) nitrate hexahydrate $Pr(NO_3)_3{\cdot}6H_2O$ was prepared by dissolving the required amount in 40 mL of deionized water under continuous magnetic stirring for 15 min. Separately, NH_4MoO_4 was dissolved in 20 mL of deionized water to obtain a clear molybdate solution. The ammonium molybdate solution was then added slowly to the praseodymium nitrate solution under constant stirring to ensure homogeneous mixing of Pr^{3+} and *Mo species*. Subsequently, an appropriate amount of NH_4Cl was introduced into the mixed solution and the suspension was stirred for an additional 30 min, which facilitated controlled precursor formation by regulating the ionic environment. The resulting mixture was transferred into a Teflon-lined stainless-steel autoclave and subjected to hydrothermal treatment at 180 °C for 12 h. After natural cooling to room temperature, the precipitate was collected by centrifugation, thoroughly washed several times with deionized water and ethanol to remove residual ions, and dried at 60 °C overnight. The final product was denoted as Pr–Mo–O.

2.2. Preparation of functionalized MWCNT (f-MWCNT)

To enhance the dispersibility of multi-walled carbon nanotubes and introduce surface oxygen-containing functional groups, pristine MWCNTs were subjected to acid functionalization. In a typical procedure, MWCNTs were refluxed in a mixed acid solution of concentrated nitric acid and sulfuric acid (HNO_3:H_2SO_4, 1:3 v/v) at 60 °C for 2 h under

continuous stirring. This oxidative treatment introduced abundant oxygenated functional groups, including carboxyl (–COOH), hydroxyl (–OH), and carbonyl (C═O) moieties, onto the surface of the nanotubes, thereby improving their hydrophilicity, surface reactivity, and electrochemical activity [40]. After completion of the reaction, the acid-treated MWCNTs were thoroughly washed with deionized water until the filtrate reached neutral pH, ensuring complete removal of residual acids. The resulting functionalized MWCNTs (f-MWCNTs) were dried at room temperature and stored for subsequent use in composite preparation.

2.3. Preparation of Pr–Mo–O@F-Mwcnt composite

To fabricate the Pr–Mo–O@f-MWCNT composite, Pr–Mo–O and functionalized MWCNTs were combined in an appropriate mass ratio (1:1) and dispersed in 40 mL of deionized water. The suspension was ultrasonicated for 45 min to ensure homogeneous dispersion and promote intimate interfacial contact between the Pr–Mo–O particles and the f-MWCNT network. During this process, the Pr–Mo–O particles were effectively anchored onto the surface of f-MWCNTs through electrostatic interactions and bonding with surface oxygen-containing functional groups. The mixture was then magnetically stirred for an additional 3 h to strengthen interfacial coupling and achieve uniform composite formation. The resulting hybrid material was collected by centrifugation, thoroughly washed with deionized water and ethanol to remove loosely bound species, and dried at 50–60 °C to obtain the final Pr–Mo–O@f-MWCNT composite. The overall synthesis route and composite formation process are schematically illustrated in Scheme 1.

2.4. Preparation of catalyst ink

For electrode modification, the catalyst ink was prepared using the as-synthesized Pr–Mo–O@f-MWCNT composite. 2 mg of composite was dispersed in 3 mL of deionized water to form a uniform suspension. The mixture was subjected to ultrasonic treatment at 200 W for 30 min to achieve a stable and homogeneous ink. Ultrasonication effectively disperses the composite, prevents agglomeration, and ensures uniform distribution of the active material, which is essential for consistent electrode coating. The freshly prepared catalyst ink was used immediately for electrode fabrication to maintain reproducibility and avoid sedimentation.

3. Results and discussions

3.1. XRD analysis

The crystalline structure and phase purity of the synthesized materials were investigated by XRD, and the corresponding patterns are presented in Fig. 1A. The Pr–Mo–O sample exhibits several sharp and intense diffraction peaks, indicating the formation of a highly crystalline oxide framework. The major diffraction reflections observed at 2θ values of approximately 28.3°, 32.7°, 47.1°, and 56.2° can be indexed to the cubic phase of praseodymium oxide (Pr_9O_{11}), corresponding to the (222), (400), (440), and (622) crystal planes, respectively, which agree well with the standard JCPDS-PDF card No 00–042–1121. In addition, several secondary reflections appearing at around 26.8°, 30.5°, and 53.4° are attributed to the (112), (004), and (224) planes of praseodymium molybdate $Pr_2(MoO_4)_3$, matching well with PDF Nos. 00–028–0861 and 00–024–0911. The coexistence of these diffraction features confirms the successful formation of a mixed praseodymium–molybdate oxide structure through strong interfacial interaction between Pr–O and Mo–O coordination units. And, no additional impurity-related diffraction peaks were detected within the instrumental limit, indicating the high phase purity of the synthesized material.

In contrast, the f-MWCNT pattern displays a broad diffraction band centered at 2θ ≈ 25–26°, attributed to the (002) plane of graphitic carbon, along with a weak shoulder near ~43° corresponding to the (101) carbon reflection. The broad nature of these features reflects the disordered graphitic stacking typical of acid-functionalized carbon nanotubes, and no additional crystalline peaks are observed, supporting the absence of inorganic impurities. For the Pr–Mo–O@f-MWCNT hybrid, the characteristic oxide reflections of Pr–Mo–O are retained, confirming that the crystalline framework of the Pr–Mo–O phase remains intact after integration with f-MWCNT. Meanwhile, the carbon (002) band is still observable in the composite, demonstrating successful incorporation of the nanotube network. Compared with pristine Pr–Mo–O, the composite shows slightly reduced peak intensities and mild broadening, which can be attributed to the dispersion of oxide domains within the carbon matrix and decreased effective crystallite coherence upon hybrid formation.

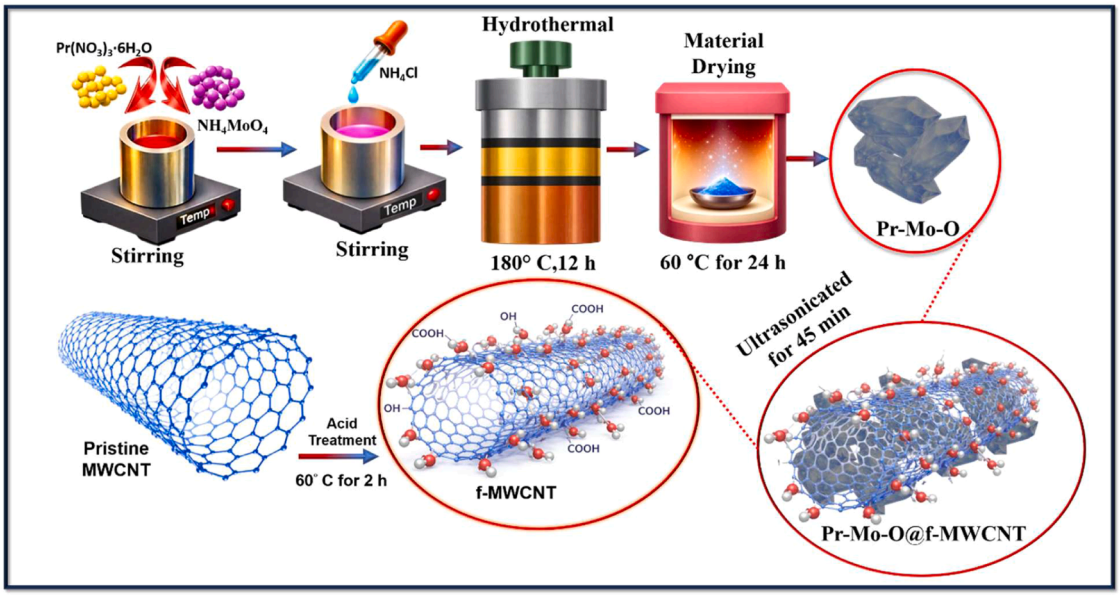

Scheme 1. Schematic representation of the synthesis of the Pr–Mo–O@f-MWCNT composite, illustrating hydrothermal formation of Pr–Mo–O, acid functionalization of MWCNTs.

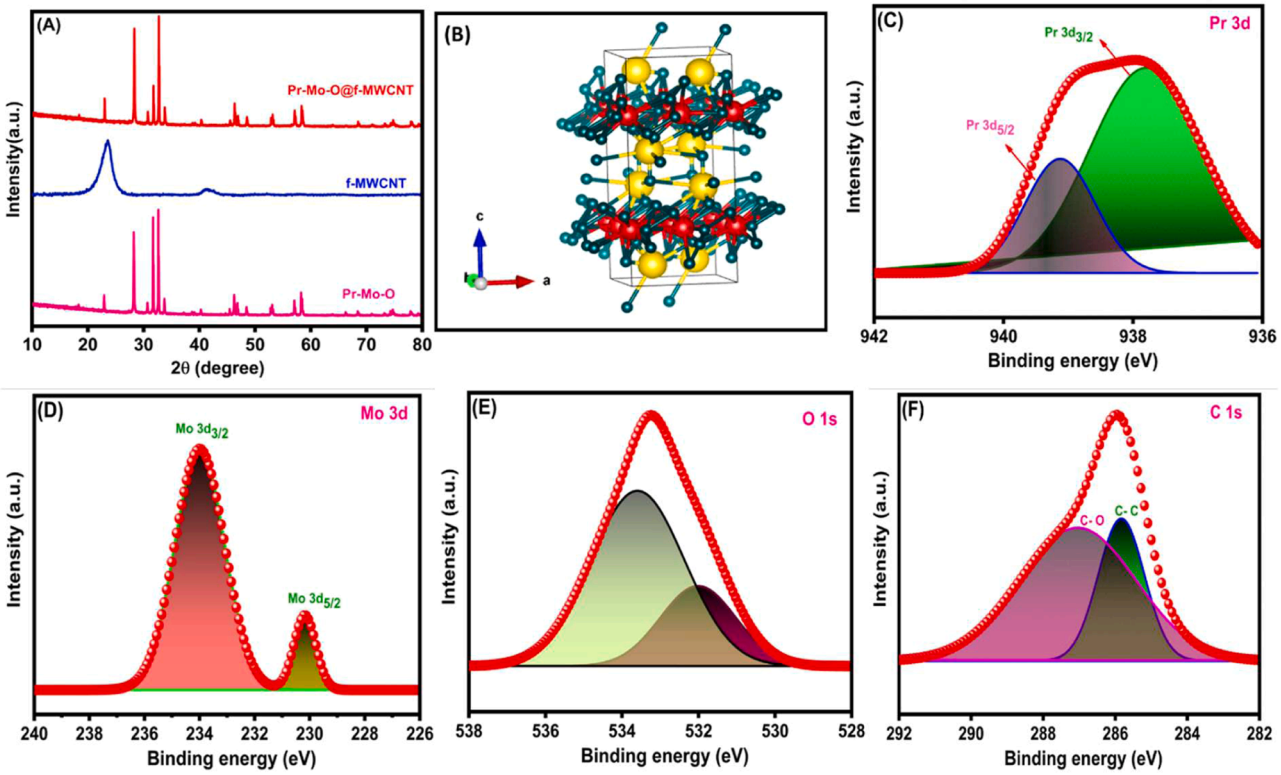

Fig. 1. illustrates the structural and surface chemical characterization of the Pr–Mo–O@f-MWCNT composite. (A) XRD patterns of Pr–Mo–O, f-MWCNT, and Pr–Mo–O@f-MWCNT confirm the formation of the Pr–Mo–O mixed oxide and its integration with the CNT framework. (B) Representative crystal structure schematic of praseodymium molybdate used for structural visualization. (C–F) High-resolution XPS spectra of Pr–Mo–O@f-MWCNT, including Pr 3d, Mo 3d, O 1 s, and C 1 s, verifying the chemical states of the constituent elements.

3.2. Crystal structure of Pr–Mo–O

Fig. 1B illustrates the representative crystal structure of the praseodymium–molybdate oxide phase used for structural visualization. The lattice is composed of praseodymium (Pr), molybdenum (Mo), and oxygen (O) atoms arranged in a three-dimensional oxide framework. In this structure, the Mo centers are coordinated by oxygen atoms to form discrete MoO_4 tetrahedral units, which act as the primary redox-active building blocks. These tetrahedra are interconnected through Pr–O coordination polyhedral, where praseodymium ions serve as structural linkers that stabilize the lattice and facilitate charge balance. The alternating arrangement of MoO_4 tetrahedra and Pr–O coordination environments generate an open and defect-tolerant framework with accessible oxygen sites. Such a structural configuration promotes efficient electron transport through Mo–O–Pr pathways and provides abundant surface-exposed oxygen atoms that can interact with electroactive species. The oxide framework and interconnected coordination network are advantageous for electrochemical applications, as they support stable redox activity, facilitate charge transfer, and enhance interfacial interactions when integrated with conductive carbon supports.

3.3. XPS analysis

The surface chemical states and elemental composition of the Pr–Mo–O@f-MWCNT composite were examined by X-ray photoelectron spectroscopy (XPS), and the high-resolution spectra are shown in Fig. 1C–F. The Pr 3d spectrum Fig. 1C exhibits two characteristic peaks at approximately 933–935 eV (Pr $3d_{5/2}$) and 953–955 eV (Pr $3d_{3/2}$), confirming the presence of praseodymium predominantly in the Pr^{3+} oxidation state, with possible minor contributions from higher-valence surface states. The Pr 3d spectrum exhibits characteristic mixed-valence features associated with the coexistence of different Pr oxidation environments, indicating complex electronic interaction within the oxide structure. The coexistence of multiple Pr valence states suggests a redox-flexible surface, which is beneficial for facilitating charge compensation and electron transfer during electrochemical operation. The Mo 3d spectrum Fig. 1D shows a well-defined spin–orbit doublet at around 232–233 eV (Mo $3d_{5/2}$) and 235–236 eV (Mo $3d_{3/2}$), characteristic of Mo^{6+} species in a molybdate-type oxide environment. Slight peak broadening indicates the presence of defect-associated Mo sites, which can promote reversible redox activity and enhance interfacial charge transport. The O 1 s spectrum Fig. 1E can be deconvoluted into lattice oxygen at ~530–531 eV, along with higher-binding-energy components (~532–534 eV) attributed to surface hydroxyl groups and defect-related oxygen species. The broadened O 1 s spectrum and asymmetric peak distribution suggest the presence of multiple oxygen-related surface environments and chemically non-equivalent oxygen species within the Pr–Mo–O framework. These non-lattice oxygen components indicate the presence of oxygen vacancies and surface-active sites, which play a crucial role in analyte adsorption and electrochemical responsiveness.

The C 1 s spectrum Fig. 1F confirms successful incorporation of f-MWCNTs, showing a dominant sp^2 C–C/C═C peak at ~284.6 eV, accompanied by oxygenated carbon species such as C–O (~286 eV) and C═O/O–C═O (~288–289 eV) introduced during acid functionalization. These functional groups enhance interfacial bonding between the Pr–Mo–O phase and the carbon framework, enabling efficient electronic coupling. Overall, the combined presence of redox-active Pr and Mo centers, defect-rich oxygen species, and a conductive, functionalized carbon network confirms the formation of a synergistic Pr–Mo–O@f-MWCNT interface [41].

3.4. FESEM analysis

The surface morphology of the synthesized materials was examined by FESEM, and the corresponding images are shown in Fig. 2A–H. The FESEM images of the Pr–Mo–O sample Fig. 2A–C reveal a densely packed nanostructured morphology composed of irregular plate-like and faceted particles that are closely assembled into compact aggregates. These oxide domains exhibit rough surfaces and sharp edges, suggesting a high density of exposed crystal facets. and it provides abundant active sites and facilitates efficient interaction with electroactive species. The higher-magnification image Fig. 2C further confirms the presence of stacked plate-like units, indicating anisotropic growth of the Pr–Mo–O phase during hydrothermal synthesis.

The FESEM image of functionalized MWCNTs (f-MWCNTs) Fig. 2D displays a highly entangled and interconnected fibrous network, characteristic of carbon nanotube assemblies. The nanotubes retain their tubular morphology after acid functionalization, while the slightly roughened surface suggests the successful introduction of oxygen-containing functional groups, which enhance interfacial compatibility with metal oxides. The morphology of the Pr–Mo–O@f-MWCNT composite is presented in Fig. 2E–H. At low magnification Fig. 2E, a well-interwoven hybrid architecture is observed, where Pr–Mo–O particles are uniformly distributed throughout the f-MWCNT network. The medium- and high-magnification images Fig. 2F–H clearly show that the Pr–Mo–O plate-like particles are firmly anchored onto and wrapped by the carbon nanotubes, forming intimate oxide–carbon interfaces. This hybrid morphology prevents severe agglomeration of the oxide phase and ensures continuous conductive pathways through the CNT network. The Pr–Mo–O nanostructures were uniformly distributed along the interconnected f-MWCNT framework with particle dimensions in the nanometer range, providing abundant exposed electroactive sites and facilitating efficient electrolyte diffusion.

3.4.1. Elemental mapping and EDX analysis

To further confirm the elemental composition and spatial distribution within the Pr–Mo–O@f-MWCNT composite, EDS elemental mapping was performed, and the results are shown in Fig. 2I–L. The elemental maps demonstrate a uniform and homogeneous distribution of praseodymium (Pr) Fig. 2I, molybdenum (Mo) Fig. 2J, and oxygen (O) Fig. 2K across the observed region, confirming the consistent presence of the Pr–Mo–O phase. The carbon (C) signal Fig. 2L, originating from the f-MWCNT matrix, is evenly distributed throughout the composite, indicating the formation of a continuous conductive framework. The strong spatial overlap of Pr, Mo, O, and C signals confirms the successful integration of the Pr–Mo–O oxide with the f-MWCNT network without noticeable phase separation or elemental clustering. In addition, the corresponding EDX spectrum Fig. S1 further verifies the presence of Pr, Mo, O, and C elements, with no detectable impurity peaks, supporting the high purity of the synthesized composite.

3.5. TEM analysis

The transmission electron microscopy (TEM) images in Fig. 3(A–J) provide detailed insight into the internal structure and interfacial architecture of the Pr–Mo–O@f-MWCNT composite. The low-magnification TEM images of pristine Pr–Mo–O Fig. 3 (A–D) reveal densely packed, irregularly shaped nano crystallites assembled into hierarchical aggregates. These oxide domains exhibit well-defined faceted edges and contrast variations, indicating polycrystalline nature and anisotropic growth during hydrothermal synthesis. Such hierarchical organization increases the density of exposed crystal facets and interparticle junctions, which are known to act as highly active electrochemical sites. The high-resolution TEM image of Pr–Mo–O Fig. 3D displays clear lattice fringes with an interplanar spacing of approximately 0.37 nm, confirming the high crystallinity of the oxide phase and consistent with the dominant praseodymium–molybdate-related planes identified in XRD. The presence of sharp and continuous lattice fringes further suggests low structural disorder within individual nanocrystals, which favors efficient charge transport across the oxide lattice.

The f-MWCNTs Fig. 3 (E–F) exhibit a characteristic hollow, multi-walled tubular morphology with smooth graphitic walls and extended one-dimensional continuity. This architecture provides long-range conductive pathways and a large interfacial area for oxide attachment, enabling rapid electron delocalization along the nanotube backbone. For the Pr–Mo–O@f-MWCNT composite Fig. 3 (G–J), the TEM images clearly demonstrate that Pr–Mo–O nanocrystals are uniformly anchored

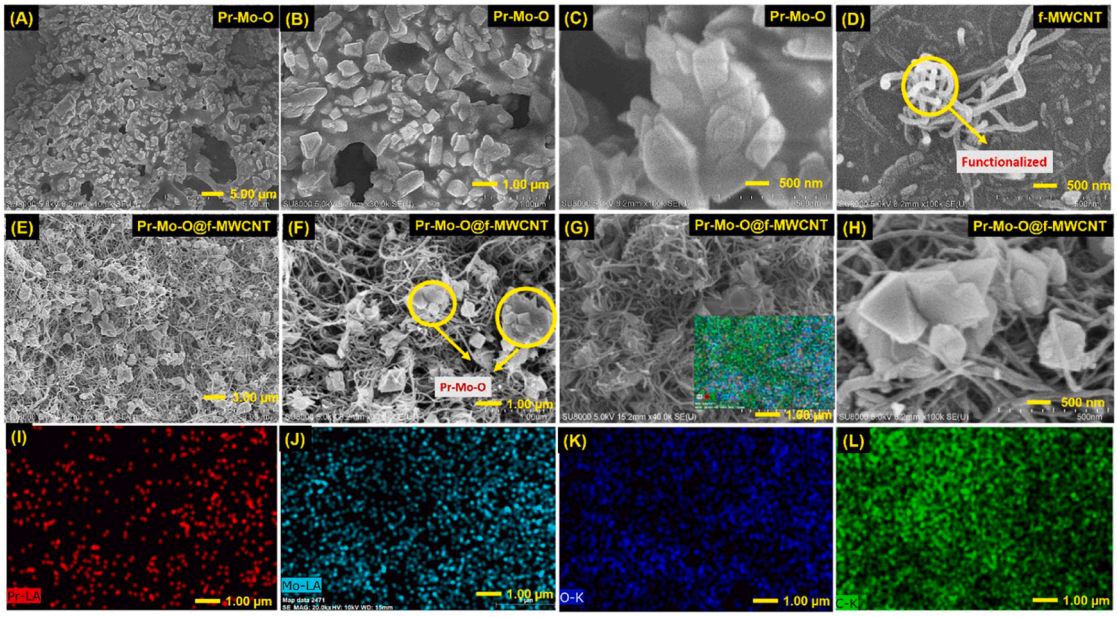

Fig. 2. shows the FESEM images and elemental mapping of the synthesized materials. (A–C) present the morphology of Pr–Mo–O, consisting of aggregated plate-like oxide structures. (D) displays the entangled fibrous morphology of f-MWCNT after functionalization. The Pr–Mo–O@f-MWCNT composite (E–H) exhibits uniform anchoring of Pr–Mo–O particles on the CNT network, forming a well-connected hybrid architecture. The corresponding EDS elemental mapping images (I–L) confirm the homogeneous distribution of Pr, Mo, O, and C throughout the composite.

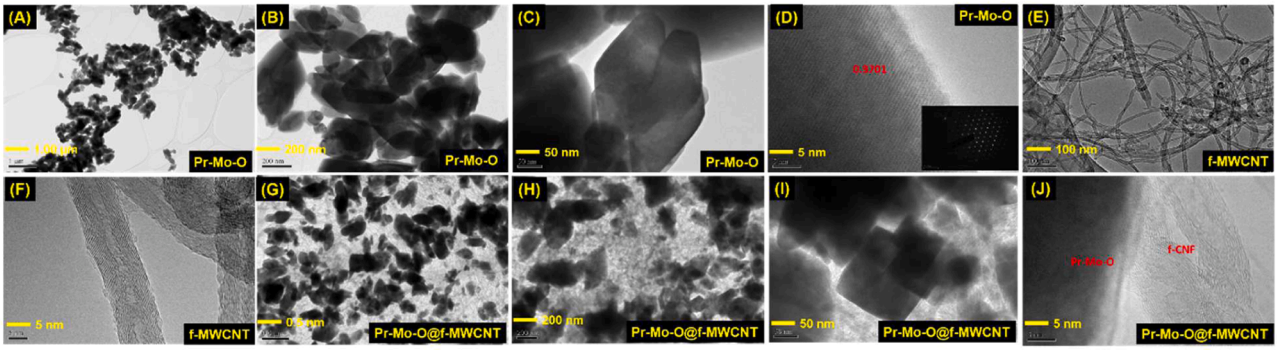

Fig. 3. TEM and HRTEM images of Pr–Mo–O, f-MWCNT, and the Pr–Mo–O@f-MWCNT composite. (A–C) Low- and high-magnification TEM images of Pr–Mo–O showing aggregated nanocrystalline oxide domains. (D) HRTEM image of Pr–Mo–O displaying clear lattice fringes with an interplanar spacing of ~0.37 nm. (E–F) TEM images of f-MWCNTs revealing the multi-walled tubular morphology and extended graphitic walls. (G–J) TEM images of the Pr–Mo–O@f-MWCNT composite illustrating uniform anchoring and intimate interfacial contact between Pr–Mo–O nanocrystals and the CNT network.

and partially wrapped by the CNT network, forming an intimate oxide–carbon heterointerface. The close interfacial contact suppresses nanoparticle agglomeration and establishes continuous electronic coupling between the redox-active oxide domains and the highly conductive carbon scaffold. This structural configuration creates a percolation network for electrons, where f-MWCNTs function as fast electron highways while the Pr–Mo–O phase supplies abundant adsorption and catalytic sites. The resulting hybrid interface is expected to significantly lower charge-transfer resistance and enhance interfacial electron/proton exchange during analyte redox processes. Collectively, the TEM and HRTEM observations provide direct nanoscale evidence of a hierarchically integrated, defect-tolerant, and electronically coupled Pr–Mo–O@f-MWCNT architecture.

3.6. Electrochemical characterization

3.6.1. Electrochemical impedance spectroscopy (EIS) analysis

Electrochemical impedance spectroscopy was performed in 0.1 M KCl containing 5 mM $[Fe(CN)_6]^{3-/4-}$ to evaluate the interfacial charge-transfer behavior of the bare and modified electrodes. The Nyquist plots Fig. 4A exhibit a well-defined semicircle in the high-frequency region corresponding to the charge-transfer resistance (Rct), followed by a linear tail in the low-frequency region associated with Warburg diffusion. The bare GCE displays the largest semicircle, with an Rct of approximately 790 Ω, reflecting sluggish electron-transfer kinetics at the unmodified carbon surface. Upon modification with Pr–Mo–O, the semicircle diameter decreases markedly to 370 Ω, indicating that the redox-active Pr/Mo centers and defect-rich oxygen environment enhance interfacial conductivity and facilitate electron exchange with

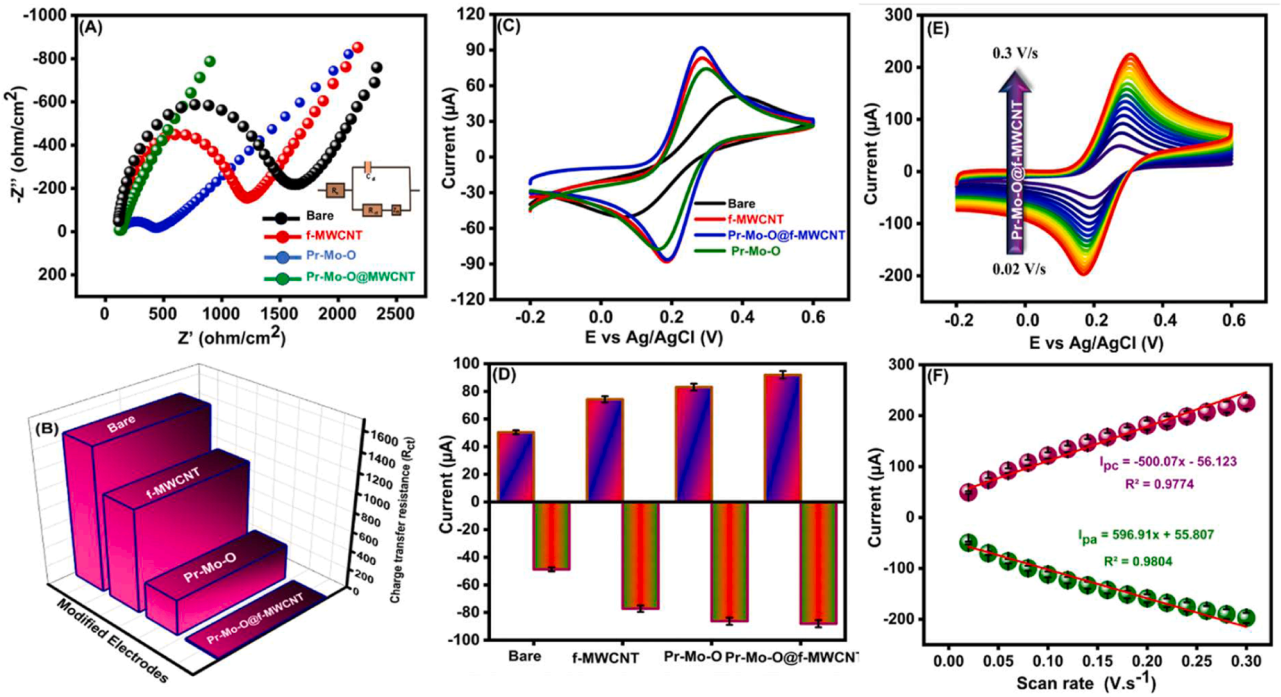

Fig. 4. Electrochemical characterization of bare GCE and modified electrodes. (A) Nyquist plots obtained from EIS measurements in 0.1 M KCl containing 5 mM $[Fe(CN)_6]^{3-/4-}$. (B) Corresponding comparison of charge-transfer resistance (Rct) values for different electrode configurations. (C) Cyclic voltammograms of bare GCE, f-MWCNT, Pr–Mo–O, and Pr–Mo–O@f-MWCNT-modified electrodes. (D) Comparison of anodic and cathodic peak currents. (E) CV responses of the Pr–Mo–O@f-MWCNT electrode at varying scan rates (0.02–0.30 V s^{-1}). (F) Linear dependence of peak currents on the square root of scan rate, indicating diffusion-controlled electron-transfer behavior.

the redox probe. A further and more pronounced reduction in Rct is observed for the Pr–Mo–O@f-MWCNT composite, reaching a value of 21 Ω, which demonstrates the superior charge-transport capability of the hybrid interface. This improvement arises from the intimate coupling between the conductive CNT network and the Pr–Mo–O phase, where f-MWCNTs act as rapid electron highways while the oxide domains provide abundant electroactive and adsorption sites. The resulting oxide–carbon heterointerface lowers the interfacial energy barrier and promotes fast electron percolation across the electrode surface. The three-dimensional impedance representation Fig. 4B highlights the descending Rct trend in the order bare GCE > f-WWCNT > Pr–Mo–O > Pr–Mo–O@f-MWCNT, confirming the synergistic enhancement of interfacial electron transfer induced by composite formation. The lower charge-transfer resistance indicates faster interfacial electron-transfer kinetics at the Pr–Mo–O@f-MWCNT-modified electrode compared with the individual components and bare GCE.

3.6.2. Cyclic voltammetry (CV) analysis

Cyclic voltammetry was carried out under identical electrolyte conditions to further probe the redox behavior and electroactive surface properties of the modified electrodes Fig. 4C. The bare GCE exhibits broad and weak redox peaks with a large peak-to-peak separation ΔEp ≈160 mV, indicating slow and quasi-irreversible electron-transfer kinetics. After modification with f-MWCNT Pr–Mo–O, the redox currents increase noticeably and ΔEp decreases to approximately ΔEp ≈130 mV and ΔEp ≈100 mV, confirming improved surface conductivity and enhanced redox mediation by the Pr/Mo centers. Notably, the Pr–Mo–O@f-MWCNT-modified electrode delivers the highest anodic and cathodic peak currents with the smallest ΔEp of about ΔEp ≈70 mV, reflecting rapid and more reversible charge-transfer behavior. This performance enhancement is attributed to the synergistic electronic coupling between the oxide phase and the CNT framework, which establishes a continuous conductive network and facilitates efficient charge delocalization and ion diffusion at the electrode–electrolyte interface. To examine the kinetic regime, CV were recorded at scan rates ranging from 0.02 to 0.20 V s^{-1} Fig. 4E. The peak currents increase linearly with the square root of the scan rate, indicating a predominantly diffusion-controlled electron-transfer process with stable quasi-reversible behavior. The smaller peak-to-peak separation observed for the Pr–Mo–O@f-MWCNT electrode indicates improved electron-transfer reversibility and accelerated electrochemical kinetics. The corresponding linear plots of anodic and cathodic peak currents versus ν Fig. 4F show strong correlation coefficients $R^2 \approx 0.9774$ and 0.9804, confirming robust and reproducible interfacial redox kinetics. The enhanced current response and reduced ΔEp for the Pr–Mo–O@f-MWCNT electrode further suggest an enlarged electroactive surface area and accelerated charge-transfer dynamics.

3.7. Electrochemical behavior and optimization studies

3.7.1. Electrochemical reaction mechanism of fenitrothion

During electrochemical sensing, fenitrothion bearing the nitro functional group (FT–NO_2) undergoes a proton-coupled electron transfer (PCET) process at the Pr–Mo–O@f-MWCNT modified electrode interface. The initial cathodic step involves a concerted four-electron and four-proton reduction of the –NO_2 moiety, Pr–Mo–O phase provides electron-rich Pr/Mo redox-active sites that facilitate the proton-coupled reduction process and accelerate interfacial charge transfer. to the formation of the corresponding hydroxylamine intermediate (FT–NHOH). Surface oxygen vacancies and defect-rich regions in the Pr–Mo–O lattice further promote fenitrothion adsorption and improve electron exchange at the electrode–electrolyte interface. This transformation is promoted by the electron-rich Pr–Mo–O catalytic domains and the highly conductive f-MWCNT network, which together lower the interfacial energy barrier and facilitate rapid charge transport. The $Pr3^{+}/Mo^{6+}$ redox centers provide transient electron-donation pathways, while surface oxygen vacancies and functional groups (–OH/–COOH) on the f-MWCNTs stabilize the adsorbed fenitrothion molecules through hydrogen bonding and π–π interactions. The proposed sensing pathway is consistent with previously reported electrochemical reduction mechanisms of nitroaromatic organophosphorus compounds [42]. Scheme 2 illustrates this detailed reaction pathway, showing the electrochemical behavior of FT on the proposed sensing platform.

3.7.2. Electrochemical response of fenitrothion at Pr–Mo–O@F-MWCNT-modified electrodes

The electrochemical behavior of FT on the bare and modified electrodes was systematically investigated to elucidate the synergistic contribution of each functional component Fig.(5A–B). The bare GCE exhibits a weak and broad cathodic response with a low peak current of approximately −13.2 μA, reflecting limited adsorption sites and sluggish electron-transfer kinetics. Upon modification with f-MWCNT, the peak current increases to about 14.7 μA, owing to the enhanced electrical conductivity and enlarged electroactive surface area provided by the conductive CNT network. Further improvement is observed for the Pr–Mo–O-modified electrode, which delivers a higher reduction current of approximately 17.4 μA, indicating that the redox-active Pr/Mo centers and surface oxygen defects facilitate stronger FT adsorption and promote catalytic electron transfer. Notably, the Pr–Mo–O@f-MWCNT composite electrode exhibits the highest cathodic current response of around −19.2 μA, confirming the formation of an efficient oxide–carbon heterointerface. The bar comparison Fig. 5B highlights the progressive increase in peak current in the order Bare < f-MWCNT < Pr–Mo–O < Pr–Mo–O@f-MWCNT, underscoring the interfacial synergy of the hybrid architecture.

3.7.3. Effect of composite loading on electrode performance

The influence of the Pr–Mo–O@f-MWCNT loading amount on the electrochemical response toward FT was examined by varying the drop-cast volume from 2 to 8 μL Fig. (5C–D). The peak current increases gradually with increasing loading and reaches a maximum at approximately 6 μL, corresponding to a well-formed, thin, and conductive composite layer that maximizes surface coverage and facilitates efficient analyte diffusion. At higher loading levels 8 μL, a slight decrease in current is observed, likely due to excessive film thickness that impedes mass transport and increases internal charge-transfer resistance. Therefore, 6 μL was selected as the optimal loading volume, providing a

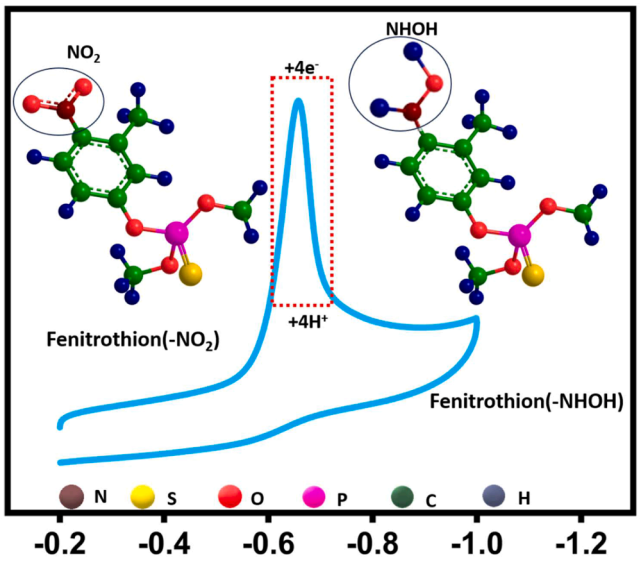

Scheme 2. illustrates the proposed multi-step reduction–oxidation pathway, highlighting the dominant four-electron/four-proton conversion of FT–NO_2 to FT–NHOH as the primary electroanalytical signal-generating step.

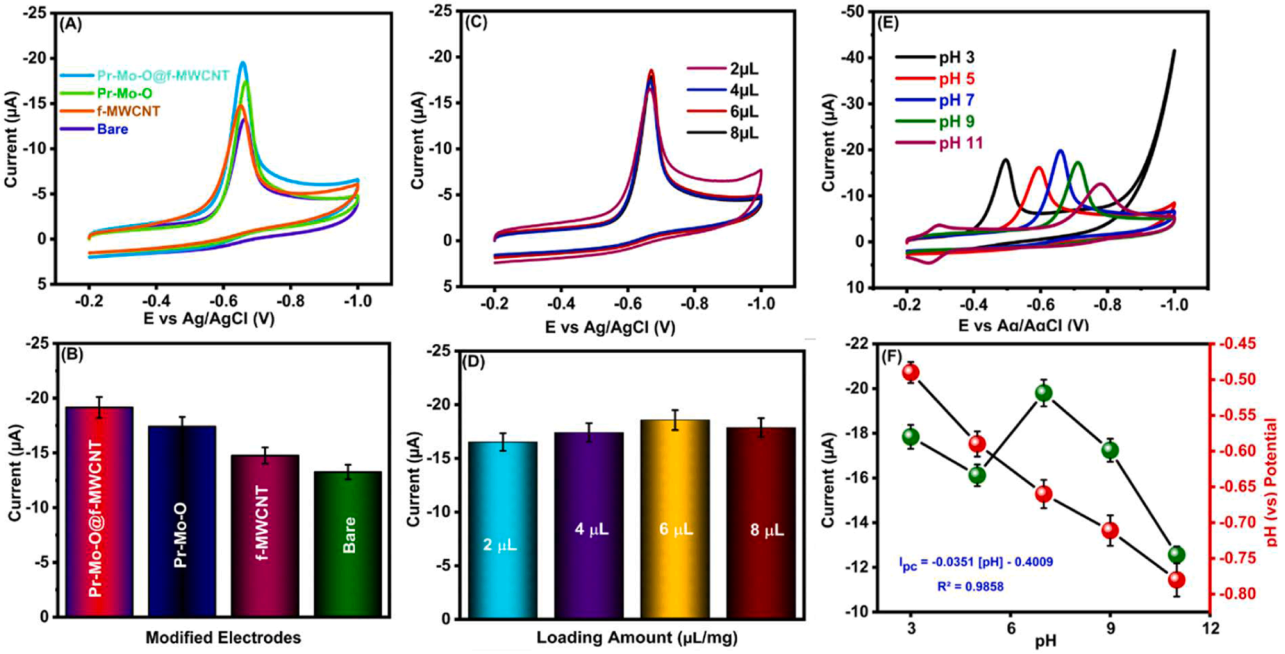

Fig. 5. Optimization of electrochemical response of the Pr–Mo–O@f-MWCNT-modified electrode toward FT. (A) CV responses of bare GCE, f-MWCNT, Pr–Mo–O, and Pr–Mo–O@f-MWCNT electrodes. (B) Comparison of peak currents for different electrode configurations. (C) Effect of composite loading volume (2–8 μL) on the electrochemical response. (D) Corresponding bar plot showing the optimized loading amount. (E) Influence of solution pH (3–11) on the DPV response. (F) Linear relationship between peak potential and pH, indicating a proton-coupled electron-transfer mechanism.

balance between active site density, electrical conductivity, and mechanical stability. The bar plot in Fig. 5D further corroborates this trend, demonstrating a clear current maximum at the optimized loading condition.

3.7.4. *Effect of pH on electrochemical response*

The effect of solution pH on the electrochemical detection of FT was investigated over a pH range of 3–11, as shown in Fig. 5E. The cathodic peak current gradually increased with increasing pH and reached its maximum response at approximately pH 7, followed by a noticeable decrease under alkaline conditions. These results indicate that proton participation plays an important role in the electrochemical reduction process of FT. At lower pH values, excessive proton concentration may influence the adsorption behavior and interfacial electron-transfer process, resulting in reduced electrochemical response. In contrast, under alkaline conditions, the decrease in current response may be associated with reduced proton availability and changes in analyte adsorption behavior at the electrode interface. The near-neutral environment provides favorable conditions for interfacial charge transfer and stable interaction between FT and the Pr–Mo–O@f-MWCNT sensing surface through hydrogen-bonding and π–π interactions. Furthermore, the experimentally obtained slope value −0.035 V/pH suggests that the electrochemical reduction process involves proton-coupled electron transfer but does not strictly follow ideal Nernstian behavior, possibly due to interfacial adsorption effects and the heterogeneous surface nature of the hybrid composite. The linear relationship between peak potential and pH. Fig. 5F, described by the fitted equation $E_P = -0.035$ pH + 0.40 ($R^2 \approx 0.985$), further confirms the direct involvement of protons in the electrochemical reaction pathway. These results identify pH 7 as the optimal condition for achieving high sensitivity, signal stability, and reliable FT detection.

3.8. *Quantitative electrochemical response toward fenitrothion*

3.8.1. *Effect of analyte concentration*

The quantitative sensing capability of the Pr–Mo–O@f-MWCNT-modified electrode toward FT was evaluated by CV in 0.1 M PBS (pH 7.0) over a concentration range of 20–100 μM at a fixed scan rate of 50 mV s^{-1} Fig. 6A. The cathodic peak current increases systematically with rising FT concentration while the peak potential remains nearly unchanged, indicating a stable and rapid interfacial electron-transfer process governed primarily by surface-mediated adsorption rather than kinetic polarization. The corresponding calibration plot Fig. 6B exhibits a strong linear relationship between peak current and FT concentration $R^2 \approx 0.98$, confirming the high quantitative reliability and sensitivity of the sensing interface. This enhanced analytical response originates from the synergistic coupling between the redox-active Pr–Mo–O phase and the highly conductive f-MWCNT network. The defect-rich oxygen lattice and exposed Pr/Mo coordination sites promote strong molecular adsorption of FT, while the one-dimensional CNT framework provides continuous pathways for rapid electron delocalization. This dual functionality establishes a highly efficient oxide–carbon heterointerface that amplifies faradaic charge transfer and suppresses resistive losses, enabling sensitive current transduction even at low analyte levels.

3.8.2. *Effect of scan rate and reaction kinetics*

The influence of scan rate on the electrochemical behavior of FT was examined in the range of 0.02–0.20 V s^{-1} Fig. 6C Both anodic and cathodic peak currents increase progressively with increasing scan rate, reflecting enhanced mass transport and accelerated charge exchange at the electrode surface. The linear dependence of peak current on the scan rate Fig. 6D, $R^2 \approx 0.99$ indicates that the electrochemical process is predominantly diffusion-controlled, with a stable quasi-reversible electron-transfer regime. At higher scan rates, a slight negative shift in the cathodic peak potential is observed, suggesting the emergence of kinetic limitations associated with interfacial charge accumulation and finite electron-transfer rates. Nevertheless, the preserved linearity and high slope values confirm strong electronic coupling across the Pr–Mo–O@f-MWCNT interface. The nanostructured architecture facilitates rapid electrolyte penetration and efficient ion accessibility, while the oxide–carbon junction lowers the activation barrier for electron migration.

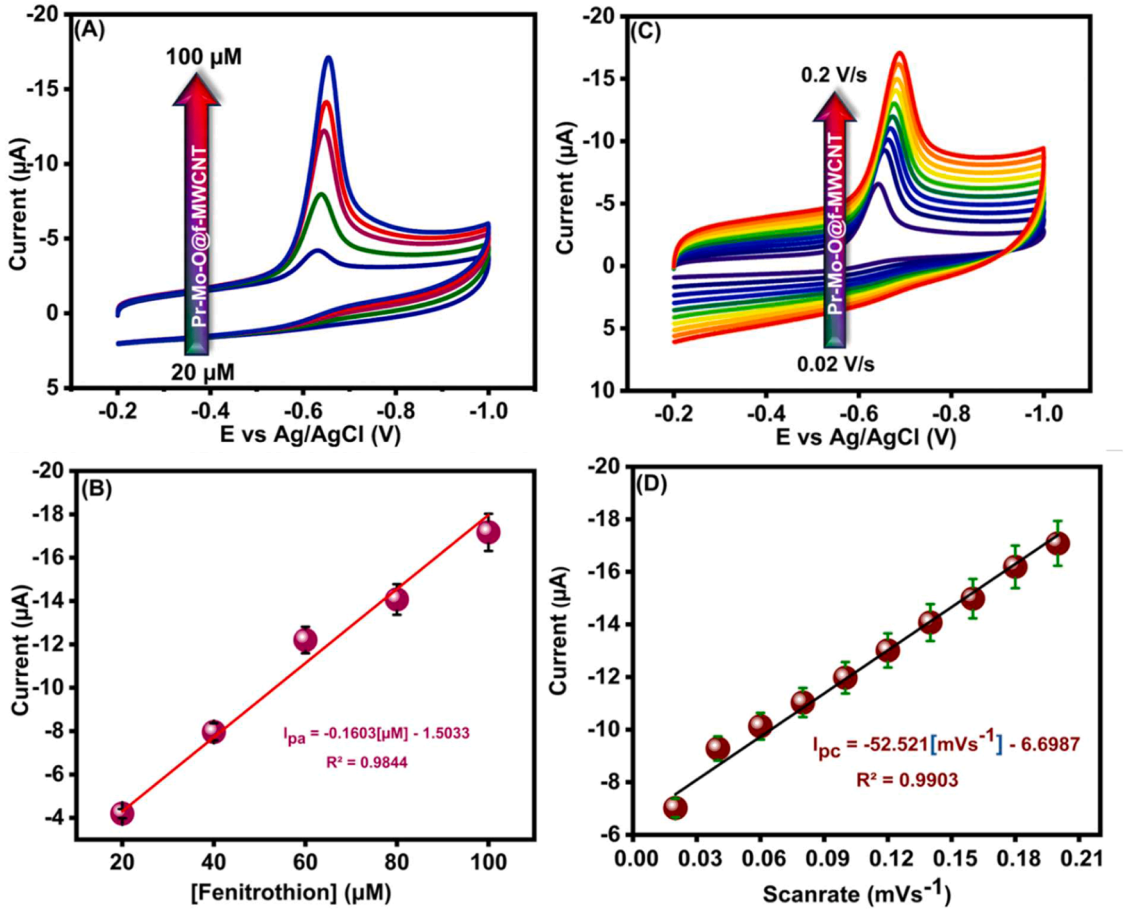

Fig. 6. Cyclic voltammetric (CV) response of the Pr–Mo–O@f-MWCNT-modified electrode toward FT. (A) CV curves recorded at increasing FT concentrations (20–100 µM). (B) Corresponding calibration plot of peak current versus FT concentration. (C) CV responses at different scan rates (0.02–0.20 V s^{-1}). (D) Linear dependence of cathodic peak current on scan rate, indicating diffusion-controlled electron-transfer behavior.

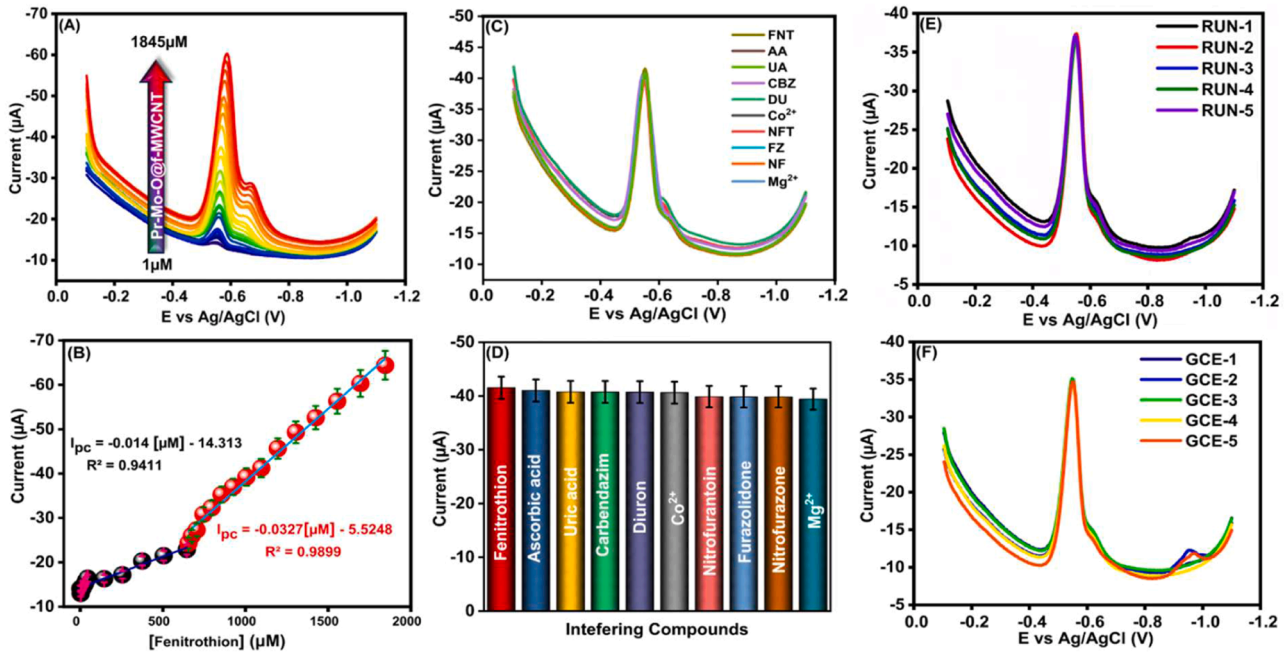

Fig. 7. Differential pulse voltametric (DPV) performance of the Pr–Mo–O@f-MWCNT-modified electrode toward FT. (A) DPV responses recorded at increasing FT concentrations (1–1845 µM). (B) Corresponding calibration plot showing two linear regimes. (C) DPV curves in the presence of common interfering species. (D) Bar comparison of current responses for FT and interferents. (E) Repeatability test using a single electrode over five consecutive runs. (F) Reproducibility evaluation across five independently prepared modified electrodes.

Collectively, these features underpin the fast redox cycling and robust quantitative performance of the proposed platform, highlighting its suitability for advanced food monitoring and trace-level pesticide analysis.

3.9. Differential pulse voltammetry sensing performance, selectivity, operational stability, and reproducibility

3.9.1. Differential pulse voltammetric (DPV) performance toward fenitrothion

The quantitative electrochemical performance of the Pr–Mo–O@f-MWCNT-modified electrode toward FT was evaluated by DPV in 0.1 M PBS (pH 7.0) over a wide concentration window Fig. 7A A progressive and well-defined increase in the cathodic peak current is observed as the FT concentration rises from 1 μM to 1845 μM, indicating stable adsorption and efficient faradaic charge transfer at the hybrid interface. The absence of peak distortion or noticeable potential drift across the entire range confirms the structural integrity of the sensing layer and the rapid electron-exchange kinetics enabled by the oxide–carbon junction. The corresponding calibration plot Fig. 7B reveals two linear regimes the first linear region at lower fenitrothion concentrations is attributed to the abundant availability of electroactive sites and rapid adsorption-assisted electron transfer at the Pr–Mo–O@f-MWCNT interface. At higher concentrations, gradual occupation of active sites and diffusion-related limitations lead to a second linear region with a different slope, reflecting a transition from surface-dominated adsorption at low concentrations to diffusion-governed transport at higher analyte levels. The regression coefficients remain high $R^2 \approx 0.94$ and 0.99, demonstrating excellent analytical linearity. The LOD was calculated using the standard Eq. 1, the limit of detection (LOD) is estimated to be 0.047 μM. This superior analytical response is attributed to the defect-rich Pr–Mo–O lattice, which provides strong molecular affinity toward FT, combined with the one-dimensional f-MWCNT network that establishes continuous, low-resistance electron pathways. Together, these features create a high-density interfacial charge-transfer network that amplifies the electrochemical signal while suppressing resistive losses. The lower concentration region was designed to evaluate the trace-level detection capability of the proposed sensing platform under environmentally relevant conditions, where FT residues are generally present at low concentrations [26].

$$\boldsymbol{LOD = 3\sigma/slope} \quad (1)$$

where σ is the standard deviation of the blank and s is the slope of the calibration curve.

3.9.2. Selectivity and interference assessment

The selectivity of the proposed sensor was examined in the presence of common electroactive and inorganic species, including ascorbic acid, uric acid, carbendazim, glucose, Co^{2+}, nitrofurantoin, furazolidone, nitrofurazone, and Mg^{2+} Fig. (7C–D). The selected interferents were chosen based on their structural similarity, electrochemical activity, and possible coexistence with fenitrothion in environmental and food-derived samples. During the anti-interference evaluation, the interferents were intentionally introduced at concentrations 10–50 times higher than that of FT to examine the robustness and competitive sensing behavior of the proposed Pr–Mo–O@f-MWCNT platform under severe interference conditions. Even at these elevated concentrations, the fenitrothion reduction signal remained clearly distinguishable with signal deviations below 2%, indicating stable anti-interference behavior of the sensing interface [43–45]. The maintained electrochemical response is likely associated with adsorption interaction between fenitrothion and the defect-rich oxygen-containing Pr–Mo–O surface together with π–π interactions between the aromatic structure of FT and the graphitic domains of the functionalized MWCNT network, which collectively promote preferential electron-transfer interaction toward FT compared with coexisting electroactive species. Although more complex matrix interferents such as humic substances and natural pigments were not investigated in the present study, the obtained results still demonstrate the reliable interference tolerance capability of the proposed sensing platform under competitive experimental conditions.

3.9.3. Operational, repeatability, and reproducibility, stability

The operational stability of the Pr–Mo–O@f-MWCNT-modified electrode was evaluated through five consecutive DPV measurements using the same electrode Fig. 7E. repeatability evaluated using five independently prepared electrodes showed RSD was found to be 0.29%, indicating excellent signal repeatability and minimal surface fouling during repeated redox cycling. This stability is attributed to the strong interfacial anchoring of the oxide nanocrystals within the CNT network, which prevents material detachment and preserves active site accessibility. Reproducibility was further assessed using five independently fabricated electrodes under identical conditions Fig. 7F. The reproducibility evaluated using five independently prepared electrodes showed resulting current responses exhibited a low RSD of 0.36%, confirming the high uniformity of the synthesis process and consistent dispersion of the hybrid nanostructure across the GCE surface. The robust electrode-to-electrode performance highlights the scalability and reliability of the proposed fabrication strategy for practical sensing applications.

The long-term storage stability of the Pr–Mo–O@f-MWCNT-modified electrode was evaluated over a 28-day period, with the corresponding DPV profiles provided in Fig. S2. The peak current and potential show negligible variation from Day 1 to Day 28, indicating strong retention of electrochemical activity and minimal surface degradation. The electrode maintained >94% of its initial response after prolonged storage, which can be attributed to the robust interfacial coupling between the Pr–Mo–O phase and the f-MWCNT network that suppresses material detachment and surface passivation. A comparison with recently reported fenitrothion electrochemical sensors is presented in Table 1. Compared with previously reported sensing systems, the proposed Pr–Mo–O@f-MWCNT platform exhibits a wider linear detection range, low detection limit, and good practical applicability in both environmental and food-derived samples. The improved sensing performance can be attributed to the synergistic interaction between the redox-active Pr–Mo–O phase and the conductive f-MWCNT network, which together enhance charge-transfer kinetics, active-site accessibility, and analyte adsorption behavior.

Table 1
Performance comparison of fenitrothion electrochemical sensors in complex matrices.

S. No	Electrode	Detection Method	Linear Range μM	LOD nM	Ref
1.	ITO/MnPc-TA/N3-PANI	SWV	0.120–15.0	49.0	[46]
2.	AuNp/en-rGO/GCE	DPV	0.360–22.5	129	[47]
3.	EC-pretreated GCE	SWV	0.400–50.0	78.0	[48]
4.	MWCNT/GCE	SWV	0.200–60.0	80.0	[49]
5.	P(Arg)-GO/PGE	SWV	0.69–20.2	173	[50]
6.	Poly (safranine)/CPE	LSV	1–15	100	[51]
7.	FCP/GCE	DPV	0.001–850	38	[42]
8.	Nano TiO_2/Nafion	DPV	0.200–4.00	90	[52]
9.	AgNp-MWCNT/GCE	ADPSV	3.60–20.22	54.0	[53]
10.	PGO/SPCE	SWV	0.02–250	61.0	[54]
11.	**Pr–Mo–O@f-MWCNT**	**DPV**	**1 −1845**	**47**	**This Work**

3.10. Real sample analysis

3.10.1. Real-sample validation and matrix-tolerant performance

To demonstrate the practical applicability and robustness of the Pr–Mo–O@f-MWCNT-modified electrode for FT detection, recovery studies were conducted using river water, soil extract, tomato, and cabbage samples as representative environmental and food matrices (Fig. 8A–H). These matrices were selected to emulate the full exposure pathway of pesticide residues from environmental reservoirs to edible crops, thereby challenging the sensor under realistic conditions involving variable ionic strength, natural organic matter, pigments, and suspended particulates.

3.10.2. Sample preparation and spiking protocol

River water was collected from a local river (Taipei Taiwan), filtered through a 0.22 μM membrane to remove suspended solids, and adjusted to PBS (0.1 M, pH 7.0) prior to analysis.

Soil samples were air-dried, sieved (<2 mm), and extracted by shaking 5 g of soil with 10 mL acetonitrile for 10 min, followed by centrifugation. The supernatant was diluted with PBS to minimize organic solvent content before spiking Soil samples were air-dried, sieved, and extracted using acetonitrile followed by centrifugation and dilution with PBS prior to analysis. Tomato and cabbage samples were homogenized (10 g), extracted with 10 mL acetonitrile, and subjected to a simple salting-out cleanup ($MgSO_4$/NaCl). After centrifugation, the organic phase was diluted in PBS to obtain a clear, electrochemically compatible extract. For each matrix, known concentrations of FT (5,10,15, and 25 μM) were added using the standard addition method, while unspiked aliquots served as negative controls. The presence of organic compounds, dissolved ions, and suspended species in real matrices may influence electrochemical response; however, the proposed sensor maintained stable and accurate signals, indicating strong matrix tolerance.

3.10.3. Electrochemical response and analytical performance

The DPV responses of the unspiked samples exhibited negligible background currents, confirming the absence of electroactive interferents native to the matrices. Upon FT addition, well-defined cathodic peaks emerged and increased proportionally with concentration across all samples Fig. 8A, C, E, and G, demonstrating stable and matrix-tolerant electron transfer at the hybrid interface. The corresponding calibration plots Fig. 8B, D, F, and H showed strong linearity $R^2 \approx$ 0.98–0.99, confirming reliable quantification in both environmental and food-derived extracts. The high recovery values 98.2–101.4% with low relative standard deviations < 2.2%, Table S1 highlight the excellent precision and reproducibility of the sensing platform. Although direct comparison with conventional instrumental techniques such as HPLC or GC–MS was not performed in the present work, the obtained recovery and reproducibility results demonstrate the practical applicability of the proposed sensing platform. Real-sample validation is a critical step for translating laboratory-scale sensors into deployable analytical tools. The consistent performance observed across chemically diverse matrices demonstrates the sensor's resistance to ionic competition, organic fouling, and pigment interference factors that often compromise electrochemical measurements in food and environmental samples.

4. Conclusion

In this work, a Pr–Mo–O@f-MWCNT hybrid composite was rationally designed and demonstrated as an efficient electrochemical sensing platform for fenitrothion. XRD, FESEM/TEM, and XPS analyses confirmed the formation of a crystalline praseodymium–molybdate oxide phase with defect-rich oxygen species and its uniform integration within the conductive CNT network, establishing a strongly coupled oxide–carbon heterointerface. This architecture significantly enhanced interfacial charge transfer and redox reversibility, enabling highly sensitive DPV detection with wide linear detection range of to 1 μM and to 1845 μM, with a low detection limit of 0.047 μM. The practical applicability of the sensor was validated in river water, soil, tomato, and cabbage samples, achieving high recoveries and stable responses, demonstrating strong matrix tolerance and operational robustness. The synergistic combination of rare-earth molybdate redox centres and MWCNT electron pathways provides a promising strategy for developing next-generation electrochemical platforms that bridge environmental surveillance and food safety monitoring of pesticide residues.

CRediT authorship contribution statement

Sri Balaji Natarajan: Writing – review & editing, Writing – original draft, Formal analysis, Data curation, Conceptualization. **Kumar Gokulkumar:** Writing – review & editing, Writing – original draft, Software, Investigation, Formal analysis, Data curation, Conceptualization. **Shen-Ming Chen:** Supervision, Resources, Project administration, Investigation, Funding acquisition, Formal analysis. **Shih-Hsuan**

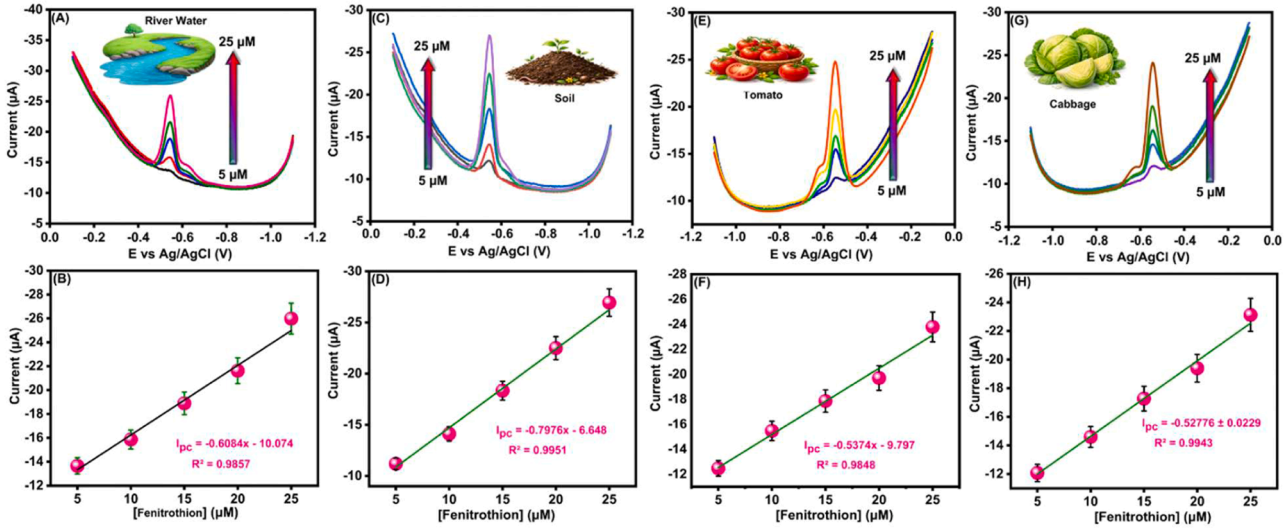

Fig. 8. Real-sample analysis of FT using the Pr–Mo–O@f-MWCNT-modified electrode. (A, C, E, G) DPV responses recorded in river water, soil extract, tomato, and cabbage samples at increasing FT concentrations (5–25 μM). (B, D, F, H) Corresponding calibration plots showing linear relationships between peak current and FT concentration for each matrix, demonstrating reliable quantification and strong matrix tolerance.

Chen: Validation, Supervision. **Kun-Mu Lee:** Resources, Investigation.

Declaration of competing interest

The authors declare that there are no known financial or personal relationships that could have influenced the work reported in this study.

Acknowledgment

The authors gratefully acknowledge financial support from the National Science and Technology Council (NSTC), Taiwan, under Project No. NSTC 111-2223-E-182-001-MY4, NSTC 114-2113-M-027-008. This research was also supported by the Chang Gung University, Taiwan. Project No (URRPD2R0011).

Supplementary materials

Supplementary material associated with this article can be found, in the online version, at doi:10.1016/j.jtice.2026.106890.

References

[1] Ahmad MF, et al. Pesticides impacts on human health and the environment with their mechanisms of action and possible countermeasures. Heliyon 2024;10(7):e29128.
[2] Carvalho FP. Pesticides, environment, and food safety. Food Energy Secur 2017;6(2):48–60.
[3] Schleiffer M, Speiser B. Presence of pesticides in the environment, transition into organic food, and implications for quality assurance along the European organic food chain–a review. Environ Pollut 2022;313:120116.
[4] Ecobichon DJ. Pesticide use in developing countries. Toxicology 2001;160(1–3):27–33.
[5] Racke KD. Environmental fate of chlorpyrifos. Rev Environ Contam Toxicol 1993:1–150.
[6] Organization, W.H.. Fenitrothion. World Health Organization; 1992.
[7] Mandal D, Mondal B, Das AK. Nucleophilic degradation of fenitrothion insecticide and performance of nucleophiles: a computational study. J Phys Chem A 2012;116(10):2536–46.
[8] Pergal MV, et al. Degradation products, mineralization, and toxicity assessment of pesticides malathion and fenitrothion. Water Air Soil Pollut 2020;231(8):433.
[9] Siddiqui SU. The effects of temperature, light and rainfall on the persistence of lindane, fenitrothion and permethrin when evaluated principally as stomach poisons against the desert locust (Schistocerca gregaria forsk.). University of Bath (United Kingdom); 1979.
[10] Şengül Demirak MŞ, Canpolat E. Plant-based bioinsecticides for mosquito control: impact on insecticide resistance and disease transmission. Insects 2022;13(2):162.
[11] Pérez-Lucas G, et al. Environmental risk of groundwater pollution by pesticide leaching through the soil profile. Pesticides-use and misuse and their impact in the environment. IntechOpen; 2018.
[12] Kookana RS, Baskaran S, Naidu R. Pesticide fate and behaviour in Australian soils in relation to contamination and management of soil and water: a review. Aust J Soil Res 1998;36(5):715–64.
[13] Rahman MS, et al. Toxic effects of fenitrothion on freshwater microcosms in Bangladesh. Toxicol Rep 2020;7:1622–8.
[14] Abdel-Ghany R, et al. Impact of exposure to fenitrothion on vital organs in rats. J Toxicol 2016;2016(1):5609734.
[15] Picó Y, Blasco C, Font G. Environmental and food applications of LC–tandem mass spectrometry in pesticide-residue analysis: an overview. Mass Spectrom Rev 2004;23(1):45–85.
[16] Falamas A, et al. A simple, rapid, and low-cost approach for colloidal nanoparticle-based surface enhanced Raman scattering detection of endosulfan pesticide at trace levels. Nano Express 2024;5(4):045006.
[17] Wilkowska A, Biziuk M. Determination of pesticide residues in food matrices using the QuEChERS methodology. Food Chem 2011;125(3):803–12.
[18] Guerrini L, Graham D. Molecularly-mediated assemblies of plasmonic nanoparticles for surface-enhanced raman spectroscopy applications. Chem Soc Rev 2012;41(21):7085.
[19] Saputra HA. Electrochemical sensors: basic principles, engineering, and state of the art. Monatshefte für Chemie-Chemic. Month 2023;154(10):1083–100.
[20] Bakker E, Telting-Diaz M. Electrochemical sensors. Anal Chem 2002;74(12):2781–800.
[21] Manimaran P, et al. Ni-metal–Organic framework/β-cyclodextrin/functionalized carbon black nanomaterials for enhanced electrochemical sensing of metronidazole in environmental and clinical samples. ACS Appl Nano Mater 2025;8(48):23260–72.
[22] Gokulkumar K, et al. Sustainable surfactant-free synthesis of MnMoO4/carbon nanofiber composite for highly sensitive detection of nimesulide in biological and pharmaceutical matrices. ACS Appl Bio Mater 2025;8(10):8864–79.
[23] Gokulkumar K, et al. Enhanced electrochemical detection of the antibiotic levofloxacin using temperature optimized Er2MoO6 nanomaterials for environmental monitoring. J Water Process Eng 2025;78:108757.
[24] Liu J, et al. α-Fe2O3/rGO composites for non-enzymatic electrochemical sensing of UA and trp and mechanism study through DFT calculation. Diam Relat Mater 2025;156:112413.
[25] Gokulkumar K, et al. Enhanced electrochemical detection of tartrazine in beverages and liquid soap via nickel phosphide-adorned functionalized carbon nanofibers. J Taiwan Inst Chem Eng 2024;157:105420.
[26] Huang S-J, et al. Nanoarchitectonics of europium vanadate nanoparticles decorated carbon nanofibers for electrochemical detection of fungicide in fruits. J Taiwan Inst Chem Eng 2024;161:105563.
[27] Huang H, Zhu J-J. The electrochemical applications of rare earth-based nanomaterials. Analyst 2019;144(23):6789–811.
[28] Jiang Y, et al. Rare earth oxide based electrocatalysts: synthesis, properties and applications. Chem Soc Rev 2024;53(2):714–63.
[29] Shaikh AA, et al. A comprehensive review of the oxidation states of molybdenum oxides and their diverse applications. Sustain Chem Environ 2024;7:100125.
[30] Shameem A, et al. Rare earth doped bismuth molybdate nanoplatelets for boosting electrochemical performance: facile synthesis and device fabrication. J Alloys Compd 2023;968:171825.
[31] Radha A, Wang S-F. Rationalization of the electrochemical behavior of praseodymium molybdates in the sensitive electrochemical reduction of nitrofuran antibiotics–furaltadone. Microchem J 2023;195:109509.
[32] Kuang W, et al. Preparation and characterization of ultrafine rare earth molybdenum complex oxide particles. J Solid State Chem 1998;140(2):354–60.
[33] Zhang GJ, et al. Microstructure and mechanical properties of multi-components rare earth oxide-doped molybdenum alloys. Mater Sci Eng: A 2008;483-484:350–2.
[34] Meskher H, et al. A review on CNTs-based electrochemical sensors and biosensors: unique properties and potential applications. Crit Rev Anal Chem 2024;54(7):2398–421.
[35] Oliveira TM, Morais S. New generation of electrochemical sensors based on multi-walled carbon nanotubes. Appl Sci 2018;8(10):1925.
[36] Li J, et al. Construction of carbon-based composites for electrochemical antibiotic sensing application: a review. J Environ Chem Eng 2026;14(2):121826.
[37] Madikere Raghunatha Reddy AK, et al. Review on advancements in carbon nanotubes: synthesis, purification, and multifaceted applications. Batteries 2025;11(2):71.
[38] Avilés F, et al. Evaluation of mild acid oxidation treatments for MWCNT functionalization. Carbon 2009;47(13):2970–5.
[39] Mallakpour S, Soltanian S. Surface functionalization of carbon nanotubes: fabrication and applications. RSC Adv 2016;6(111):109916–35.
[40] Gokulkumar K, Priscillal IJD, Wang S-F. Deep eutectic solvent-mediated synthesis of PDA coated f-CNF doped ZnS nanoparticles for electrode modification: innovative sensing platform for determination of pollutant 3-nitrophenol. J Alloys Compd 2022;924:166561.
[41] Prakash K, et al. Rational design of novel 3D flower-like praseodymium molybdate anchored graphitic carbon nitride: an efficient and sustainable photocatalyst for mitigation of carcinogenic pollutants. Appl Surf Sci 2021;569:151104.
[42] Jeyaraman A, et al. Hard template assisted synthesis of iron-cobalt phosphide core-shell for the enhanced electrochemical detection of fenitrothion. Chem Eng J 2024;491:151642.
[43] Edwin DSS, et al. Electrochemical analysis of indigo carmine using polyarginine modified carbon paste electrode. J Electrochem Sci Eng 2021;11(2):87–96.
[44] Bhimaraya K, et al. Detection of levofloxacin using a simple and green electrochemically polymerized glycine layered carbon paste electrode. Chemosensors 2023;11(3):191.
[45] Manjunatha J, Osman SM, Ataollahi N. Electrochemical polymerized DL-phenylalanine modified carbon nanotube sensor for the selective and sensitive determination of caffeic acid with riboflavin. Sci Rep 2024;14(1):30950.
[46] KOCA, A., An electrochemical sensor for the detection of pesticides based on the hybrid of manganese phthalocyanine and polyaniline. 2019.
[47] Shams N, et al. Electrochemical sensor based on gold nanoparticles/ethylenediamine-reduced graphene oxide for trace determination of fenitrothion in water. RSC Adv 2016;6(92):89430–9.
[48] Geremedhin W, Amare M, Admassie S. Electrochemically pretreated glassy carbon electrode for electrochemical detection of fenitrothion in tap water and human urine. Electrochim Acta 2013;87:749–55.
[49] Soltani-Sarvestani M, et al. A novel preconcentration/extraction method for fenitrothion residues and its electrochemical sensing in pistachio kernels. J Mater Sci: Mater Electron 2020;31(14):11268–75.
[50] Bolat G, et al. Poly-arginine/graphene oxide functionalized disposable sensor for monitoring fenitrothion pesticide residues in water and cucumber samples. Mater Today Chem 2023;30:101517.
[51] El-Hallag IS, Moharram YI, Selim SM. Poly (safranine) modified carbon paste electrode as a sensor for the determination of fenitrothion pesticide. Sci Rep 2023;13(1):14332.
[52] Kumaravel A, Chandrasekaran M. A biocompatible nano TiO2/nafion composite modified glassy carbon electrode for the detection of fenitrothion. J Electroanal Chem 2011;650(2):163–70.
[53] Khan I, et al. Fabrication of electrochemical nanosensor based on polyaniline film-coated AgNP-MWCNT-modified GCE and its application for trace analysis of fenitrothion. Ionics 2017;23(5):1293–308.
[54] Balasubramanian K, et al. Highly sensitive detection of environmental toxic fenitrothion in fruits and water using a porous graphene oxide nanosheets based disposable sensor. Env Res 2024;259:119500.